International Journal of Heat and Fluid Flow 30 (2009) 1171–1182

Contents lists available at ScienceDirect

International Journal of Heat and Fluid Flow

journal homepage: www.elsevier.com/locate/ijhff

Two-phase pressure drop and flow visualization of FC-72 in a silicon microchannel heat sink

Ayman Megahed, Ibrahim Hassan *

Department of Mechanical and Industrial Engineering, Concordia University, Montreal, Quebec, Canada H3G 1M8

ARTICLE INFO

Article history:
Received 31 March 2009
Received in revised form 26 June 2009
Accepted 29 July 2009
Available online 9 September 2009

Keywords:
Heat sink
Two-phase flow
Pressure drop
Flow visualization

ABSTRACT

The rapid development of two-phase microfluidic devices has triggered the demand for a detailed understanding of the flow characteristics inside microchannel heat sinks to advance the cooling process of micro-electronics. The present study focuses on the experimental investigation of pressure drop characteristics and flow visualization of a two-phase flow in a silicon microchannel heat sink. The microchannel heat sink consists of a rectangular silicon chip in which 45 rectangular microchannels were chemically etched with a depth of 276 μm, width of 225 μm, and a length of 16 mm. Experiments are carried out for mass fluxes ranging from 341 to 531 kg/m^2 s and heat fluxes from 60.4 to 130.6 kW/m^2 using FC-72 as the working fluid. Bubble growth and flow regimes are observed using high speed visualization. Three major flow regimes are identified: bubbly, slug, and annular. The frictional two-phase pressure drop increases with exit quality for a constant mass flux. An assessment of various pressure drop correlations reported in the literature is conducted for validation. A new general correlation is developed to predict the two-phase pressure drop in microchannel heat sinks for five different refrigerants. The experimental pressure drops for laminar-liquid laminar-vapor and laminar-liquid turbulent-vapor flow conditions are predicted by the new correlation with mean absolute errors of 10.4% and 14.5%, respectively.

1. Introduction

Developments in semiconductor technology have made it possible for extraordinary advances in the miniaturization of devices. Recently, there have been drastic increases in the heat density of integrated circuits due to rapid improvements in their speed and size. As a result, heat removal has become an important factor in the advancement of micro-electronics due to the increased current–voltage handling capability of power electronic devices (Bergles, 2003).

Over the past decade or so, many research groups used micromachining technologies to develop different types of microfluidic devices in a variety of different materials, such as silicon, glass, quartz, and plastics. The large surface-to-volume ratios of microchannels make them excellent candidates for efficient heat transfer devices. More recently, research has been intensified on the use of microchannel heat sinks as a viable technology to resolve the thermal challenges of the next generation of high heat flux devices. This MEMS-based cooling device has potential applications in the cooling of integrated circuits and the thermal management of operating systems, across a broad range of industries such as computer, biomedical, automotive, and aerospace.

Studies in microchannel heat transfer demonstrated the potential possibilities of thermal control of electronic devices. Early experimental studies, such as that carried out by Tuckerman and Pease (Tuckerman and Pease, 1981) in the early 1980s, show that electronic chips can be cooled effectively using forced convection by running water through parallel microchannels mounted directly on the back of a circuit board. The microchannel cross-sections were rectangular, and ranged in height from 50 μm to 56 μm and in width from 287 μm to 320 μm. Their work is considered to be a milestone in the development of microscale heat sinks, and this initial study has led to continued research on microchannel heat transfer that will eventually lead to the development of high performance micro-heat exchangers.

Flow boiling heat transfer in microchannels has received growing attention in recent years due to the efficiency in heat transfer of two-phase flow compared to single-phase flow. The major advantages stem from the latent heat which allows for a reduced flow rate while achieving a higher heat transfer coefficient and also allows constant coolant temperature in the stream-wise direction. Lee and Lee (2001) investigated adiabatic two-phase flow pressure drop in horizontal rectangular mini and macrochannels using air and water as working fluids. A new correlation for two-phase pressure drop in horizontal mini and macrochannels was proposed by correlating the two-phase multiplication factor to the viscous, surface tension, and inertia effects. This correlation can be used

* Corresponding author.
E-mail address: ibrahimh@alcor.concordia.ca (I. Hassan).

0142-727X/$ - see front matter © 2009 Elsevier Inc. All rights reserved.
doi:10.1016/j.ijheatfluidflow.2009.07.006

Nomenclature

A_{ch}	microchannel heat transfer area, m^2
C	two-phase multiplication factor
Co	confinement number
C_p	specific heat, J/kg °C
D	diameter, m
dP/dL	pressure gradient, Pa/m
f	friction factor
G	mass flux, kg/m^2 s
H_{ch}	channel height, m
h_{fg}	latent heat of vaporization, J/kg
$K(\infty)$	Hagenbach's factor
K	loss coefficient
L	length, m
MAE	mean absolute error
$\dot{m}$	mass flow rate, kg/s
N	total number of data points
N_{ch}	total number of channels
ΔP	pressure drop, Pa
Q	heat, W
q	net heat flux, W/m^2
Re	channel Reynolds number
T_{in}	manifold inlet temperature, °C
T_{sat}	saturation temperature, °C
u	velocity, m/s
v	specific volume, m^3/kg
We	Weber number
W_{ch}	channel width, m
x_e	vapor quality
X^2	Martinelli parameter
c,c_1,c_2,c_3	constants of Eq. (23)

Greek symbols

α_o	void fraction
β	channel aspect ratio
μ	dynamic viscosity, N s/m^2
ρ	density, kg/m^3
σ_{ch}	area ratio
λ	dimensionless group in Table 3
ψ	dimensionless group in Table 3
ϕ_f	Two-phase pressure drop multiplier

Subscripts

90	90° bend
a	acceleration component
axial	axial heat loss
c	contraction
ch	channel
con	convection heat loss
dyn	dynamics
en	enlargement
expt	experimental
f	liquid
fg	liquid–vapor
fo	liquid only
fr	frictional component
g	vapor
gr	gravitational component
h	hydraulic
i	input
loss	heat loss
net	net heat
o	outlet
pred	predicted
rad	radiation heat loss
sat	saturated
sp	single-phase
sub	sub-cooled
tot	total
tp	two-phase

to predict the pressure drop in microchannels for a wide range of Martinelli parameter and Reynolds number. The correlation was validated by 305 data points obtained for four different hydraulic diameters (780, 1910, 3640, and 6670 μm). Earlier, Mishima and Hibiki (1996) presented data for flow regime, void fraction and pressure drop for an air–water flow in capillary tubes with an inner diameter in the range of 1000–4000 μm. It was found that capillary force is important in describing the bubble shape.

Additional experimental studies have focused on two-phase pressure drop in microchannels. Lee and Mudawar (2005) published an extensive experimental investigation into flow boiling pressure drop in microchannels under high mass flux and high heat flux conditions, using R-134a as the coolant. Their test section consisted of 53 parallel, and presumably identical, rectangular channels, with a nominal cross-section of 231 μm by 713 μm, constructed into an oxygen-free copper block. The channels were 2.5 cm long, and were all connected to a large plenum at the inlet and outlet. They proposed new correlations to predict the two-phase flow pressure drop for R-134a and water as a function of Reynolds number and Weber number.

A subsequent study of Garimella and Chen (2006) examined the heat transfer coefficient and pressure drop of a dielectric fluid for flow boiling through a microchannel heat sink. The heat sink consists of 24 microchannels, each of which was 389 μm wide and 389 μm deep. The flow rate range was 35 to 60 ml/min for a heat flux ranging from 542 to 730 kW/m^2. They indicated that bubbly flow was dominant at low heat fluxes. At high heat fluxes, the flow regimes in the downstream portion of the microchannels indicated that alternating wispy-annular flow and churn flow were the dominant mechanisms. The authors found that both the heat transfer coefficient and pressure drop increase with increasing heat flux.

Lee and Garimella (2008) reported experimental data on pressure drop characteristics for deionized water flow through a silicon microchannel heat sink with 25 integrated micro-temperature sensors. They found that since the Lockhart and Martinelli correlation was developed for adiabatic and turbulent-liquid turbulent-vapor flow, it gives poor predictions in microchannls two-phase flow of imposed heat flux. A new correlation was developed to predict the two-phase pressure drop by considering the effect of mass flux and hydraulic diameter after a critical assessment to five correlations available in the literature.

Considerable attention has been given to flow pattern visualization within the microchannels (i.e., Jiang et al., 2000; Jiang et al., 2001 and Lee et al., 2003). Several flow pattern maps have been performed previously to predict flow transitions and flow regimes for microchannels by Revellin and Thome (2007) and for micro-heat exchange applications by Balasubramanian and Kandlikar (2005).

Revellin and Thome (2007) developed a diabatic pattern map model for two-phase flow in microchannels. Their map can be used to predict the transition between different flow regimes. They measured flow pattern data and bubble frequency of diabatic R-134a and R-245fa flows in 509 and 790 μm diameter glass channels using two laser beams. They suggested that the transition

from bubbly to slug flow is dominated by effect of the boiling number. The flow pattern map indicated that flow regimes observed at low mass flux are primarily annular and include slug and bubbly-slug regimes.

A comprehensive study by Hetsroni et al. (2004) investigated convective boiling flow of clear water with surfactant for different flow patterns. Microchannel cross-sections in the shape of isosceles triangles were fabricated in a silicon substrate. The studied channels' base width ranged from 200 μm to 310 μm, while the angles at the base were 55°. The authors employed a microscope and high-speed digital video imaging to visualize incipience of individual bubbles, bubble growth, flow patterns, and the motion of vapor–liquid flow. It was found that the bubble slug velocity is higher than the liquid-phase velocity in the film region.

All the experimental investigations and correlations of two-phase frictional pressure drop, reported in the literature, are based on data from microchannels with hydraulic diameters larger than 349 μm. The two-phase pressure drop characteristics and applicability of correlations of frictional pressure drop to a rectangular microchannel with a smaller hydraulic diameter has not yet been investigated, and needs to be clarified.

The principal objective of the present work is to investigate experimentally the pressure drop characteristics of two-phase laminar-liquid laminar-vapor flow in 45 parallel microchannels with a hydraulic diameter of 249 μm. Pressure drop results are presented for two-phase flow of FC-72 as a function of exit quality and heat flux. Flow visualization allows for the determination of flow regimes in addition to characterizing the transient patterns that exist in different channels because of the inlet manifold configuration. Finally, the development and validation of a generalized pressure drop correlation for different refrigerants in microchannels is introduced after a critical assessment of the available correlations in the literature. The new correlation was verified with two extensive data sets from the literature in addition to the experimental data presented in this paper.

2. Experimental investigation

2.1. Test facility flow loop

The experimental flow loop used in the present study is shown in Fig. 1, and is the same used by Muwanga et al. (2007). The working fluid in the present investigation is FC-72 (3M), a low viscosity electronics cooling fluid widely used in the industry, whose properties are shown in Table 1. Advantages of FC-72 are that it has a relatively low boiling point (56.1 °C at 1 atm) and dynamic viscosity (6.4×10^{-4} N s/m^2 at 25 °C). Moreover, it has a high dielectric constant so it will not damage the electronic components in case of leakage. However, it has very large air solubility, and therefore requires degassing prior to flow boiling experiments to eliminate non-condensable air from the working fluid.

The fluid operates in a closed system and is continuously circulated by means of a magnetically coupled gear pump (Cole-Parmer), as shown in Fig. 1. The gear pump operates at a controlled speed and supplies a maximum flowrate of 290 ml/min, with a pressure of 517 kPa. Downstream from the pump is a 15 μm filter, to remove any particles within the flow. The system flowrate was monitored by means of a nutating digital output flowmeter (DEA Engineering), and operates at a flowrate range from 10 to 250 ml/min.

Prior to entering the test section, the fluid enters a preheater for additional flow temperature control. The preheater is a counter flow, tube-in-tube heat exchanger with distilled water as the heating fluid. The FC-72 enters the test section at a temperature 2 °C below its saturation temperature and exits as two-phase. As shown in Fig. 1, the test section is heated by means of Joule heating with the use of a power supply. After flowing through the test section, the FC-72 is partially condensed in the tubing on its way to the tank. Also apparent from the figure are the image and data acquisition systems, details of which will be explained in a later section.

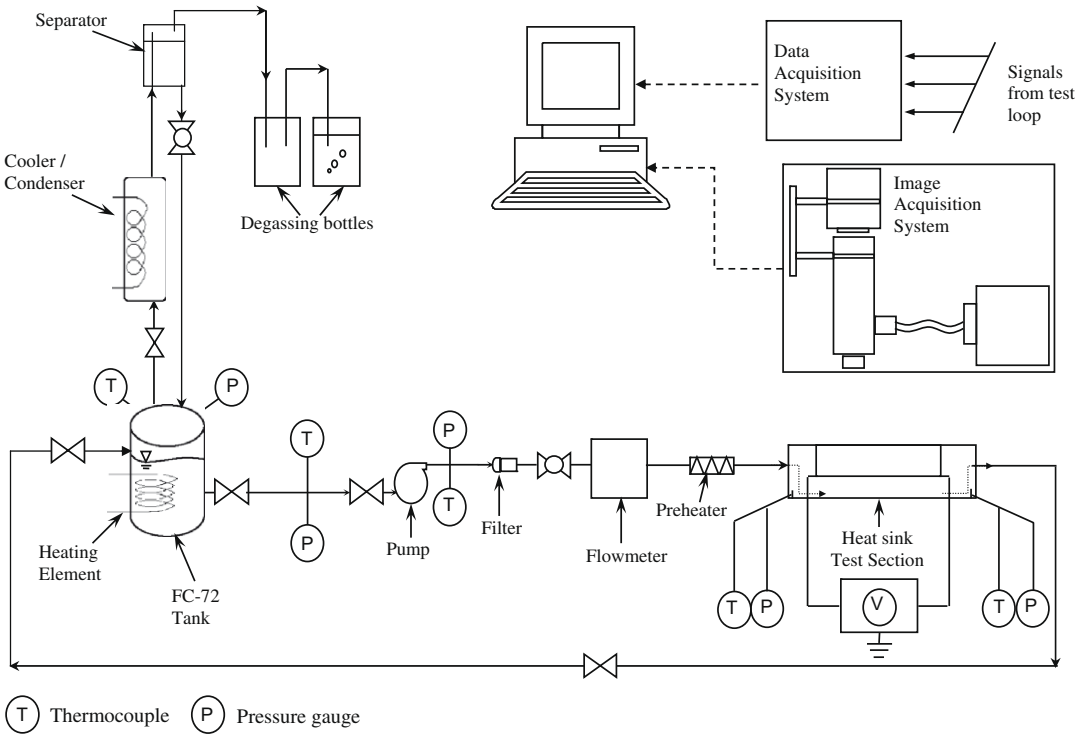

Fig. 1. Experimental test facility flow loop.

Table 1
Properties of FC-72 at 25 °C and 1 atm.

Parameter	Value
ρ	1680 kg/m^3
μ	6.4×10^{-4} N s/m^2
C_p	1100 J/kg°C
σ	0.01 N/m
T_{sat}	56.1 °C
h_{fg}	88 kJ/kg
Dielectric constant	1.75

The degassing procedure is carried out to purge the system of air. As shown in the flow loop schematic (Fig. 1), directly above the FC-72 tank is the degassing flow loop, which consists of valves, a water cooled condenser, a separator, and degassing bottles. With the test section installed, the fluid is circulated through the system at a high flow rate (~50 ml/min). Through the use of the heating element, the FC-72 tank is heated until the fluid in the tank is boiling (~60 °C). The preheater, just upstream of the test section, is also turned on to maintain the fluid at a high temperature throughout the system, above 50 °C. The valves to the degassing flow loop are then opened, which allows the vapor from the FC-72 tank to travel through the condenser and condense. The condensed fluid then flows to a separator, where the heavier liquid is returned to the tank, and the air is released to the degassing bottles. The fluid is circulated for about 1 h, allowing the entire fluid to pass through all elements of the system. Once the fluid is degassed, the system is left to cool down, and the FC-72 vapor in the tank is allowed to condense.

2.2. Test section

The test section used in the present study consists of the silicon heat sink including a resistance heater deposited on the back, and an acrylic support for laboratory manipulations. The microchannel heat sink is designed as an integrated microsystem consisting of an etched silicon wafer, a Pyrex cover plate, and platinum heater strips. (Fig. 2)a and b shows photographs of the microchannel heat sink used in the present experiment, with top and bottom views.

The etched silicon wafer consists of a rectangular silicon chip in which 45 rectangular microchannels (Fig. 2a) were etched using Deep Reactive Ion Etching (DRIE). Microchannels were realized by bonding the Pyrex cover anodically to the silicon wafer resulting in the fourth wall to close the channels, which also providing a transparent cover for flow visualization. The Pyrex cover also has an inlet and outlet hole, each of which is 1 mm in diameter, as shown in Fig. 2a. These holes extend to the inlet and outlet manifolds of the heat sink. They introduce a high pressure drop. However, the inlet hole serves as a throttling valve before the fluid enters the test section to reduce flow instabilities (Kandlikar, 2002). The integrated heater (Fig. 2b) is deposited onto the backside of the silicon wafer under the microchannels to provide a uniform heat flux. The length of the heater strip is 186 mm and it has a width of 1 mm. The serpentine heater was designed for a nominal resistance of 240 Ω with a potential applied serially through the entire length of the serpentine. (Fig. 3)a presents a schematic for the heat sink dimensions. As shown in this figure, the inlet and outlet manifolds were designed with tapered walls to provide better flow distribution throughout the entire channel array. (Fig. 3)b

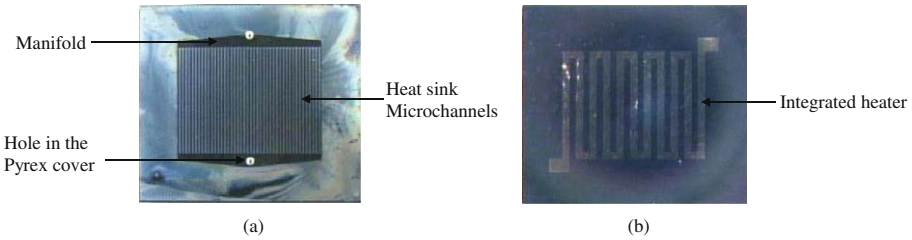

Fig. 2. A photograph of the fabricated straight microchannel heat sink with (a) microchannels and Pyrex cover, (b) integrated heater on the back.

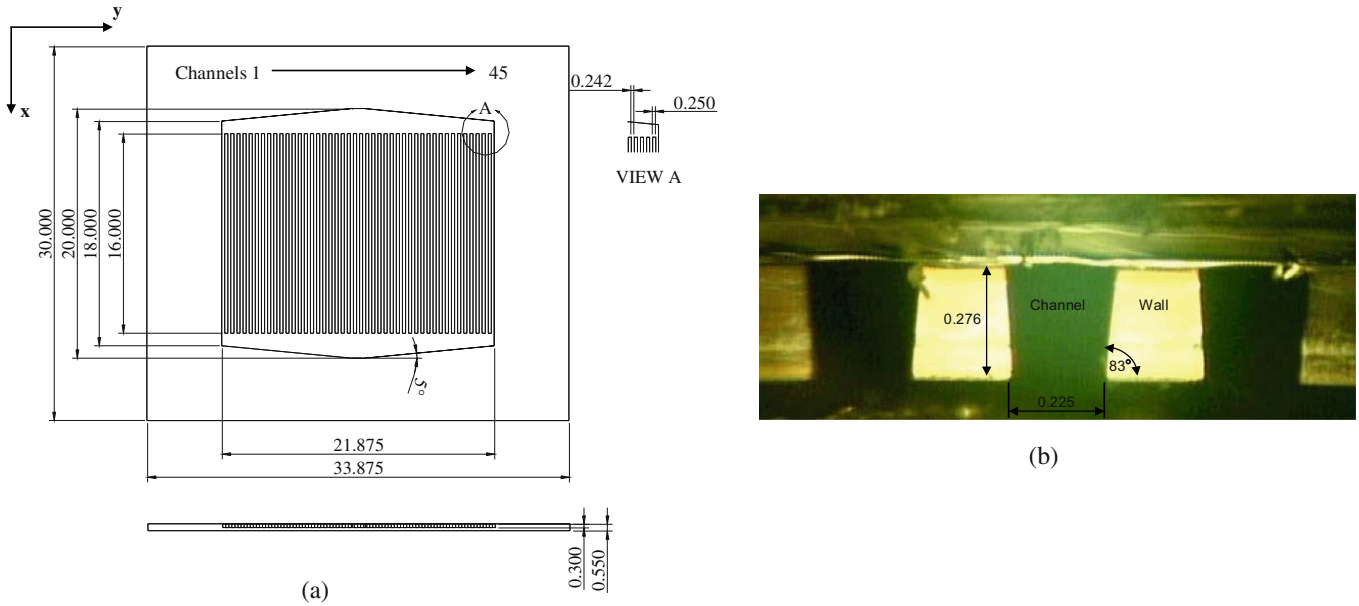

Fig. 3. (a) Detailed schematic of microchannel heat sink, (b) cross-section for the microchannels showing actual cross-sectional area and dimensions (dimensions are in mm).

shows a cross-section of the microchannels. It shows that the actual cross-section of the microchannel is not perfectly rectangular, but close to trapezoidal. Each channel has a depth of 276 μm and a width of 225 μm, as shown.

The heat sink is mounted on an acrylic support (Fig. 4) designed to provide a rigid base for the heat sink and to create inlet and outlet plenum chambers to measure the fluid bulk temperature and static pressure. Also, a cavity is machined on the backside of the support to allow for flow visualization within the channels. To adequately seat the heat sink in the support, the acrylic support possesses a groove with a depth of 0.3 mm, and an area similar to that of the footprint area of the heat sink (30 mm × 33.875 mm). The inlet and outlet holes of heat sink's Pyrex cover are precisely aligned with the holes machined in the acrylic support. The heat sink is bonded to the support using a high temperature epoxy.

2.3. Measurement methods

Two 1.5 mm diameter Type-T (Omega) thermocouples were placed in each plenum chamber of the test section (see Fig. 4) to measure the bulk fluid temperature. Two static pressure transducers tracked the gage pressure in the inlet and outlet plenums, with ratings of 517 kPa (75 psi) and 345 kPa (50 psi), respectively. The output from these and other sensors was monitored through an automated data acquisition system using LabVIEW™ software. Image acquisition was carried out in LabVIEW and the images were captured in Red–Green–Blue (RGB) format.

A schematic of the image acquisition system is shown in Fig. 5. Light from an illuminator box (Optem Intl.) is directed through a fiber optic cable, keeping the heat generated from the light source away from the test section. From the figure, it is shown that the light is passed through a polarizer prior to entering the zoom lens casing, where it is deflected to the test surface by a beam splitter. Upon reflection from the coated surface, the light is circularly polarized and is passed into the zoom lens through the analyzer, and is directed to the CCD camera.

Through the use of an LCD television, real time monitoring and positioning of the test section was possible. This allowed the operator to precisely align the test section. The video signal used in the television loop comes from a separate output line directly from the camera. Flow visualization is obtained using a Sony 3-CCD analog camera (model DXC-9000) connected to a variable zoom microscopic lens at 1/10,000 shutter speed. This combination is mounted onto a three-axis traverse, equipped with variable length stages with 1 μm resolution. The lateral and vertical axis stages allow for fine-tuning of both focusing and positioning. A high resolution objective lens 10×(Optem) provided a higher magnification to allow optical access inside the microchannels. Using this objective lens, the resolution of the images was increased to 3.3 microns/pixel.

2.4. Experimental parameters and procedure

To begin the measurements, the heating element in the FC-72 tank is adjusted to maintain the tank temperature at 50 °C, and the preheater is adjusted to raise the fluid temperature until the inlet fluid bulk temperature was just 2 °C below its saturation temperature (~54 °C). The flow rate is measured and held constant for each set of data collected. Measurements were carried out for five different mass fluxes ranging from 341 to 531 kg/m^2 s. After

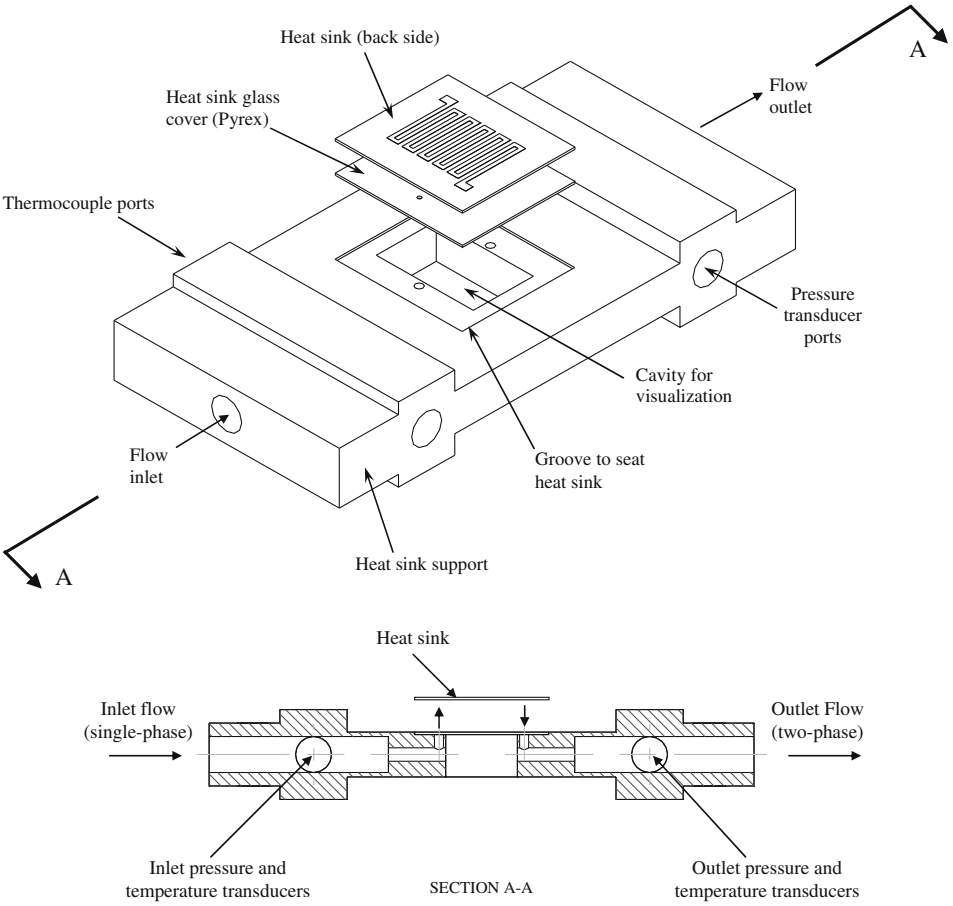

Fig. 4. Microchannel heat sink mounted on the acrylic support.

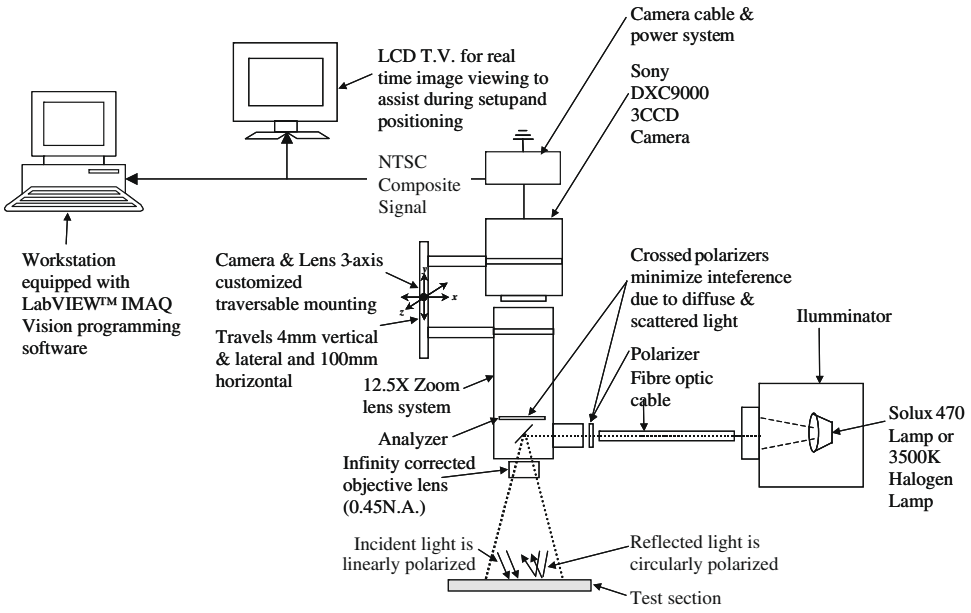

Fig. 5. Schematic of the image acquisition system.

running the flow through the system, measurements were ready to be taken and the voltage from the power supply (Joule heating) was turned on. The experimental conditions are presented in Table 2.

Uncertainty propagation was evaluated using the methods outlined by Kline and McClintock (1953). Uncertainties in pressure drop and thermocouple measurements are 1.3% and ±0.72 °C, respectively, based on instrument specifications. The uncertainty in flow rate was estimated at 6.1% Uncertainty in the heat sink hydraulic diameter is based on the manufacturing tolerance at 5.1 μm.

2.5. Data reduction

The total pressure drop across the heat sink can be expressed as:

$$\Delta P_{tot} = \Delta P_{sp} + \Delta P_{tp}, \tag{1}$$

where ΔP_{tot} is the sum of single-phase and two-phase pressure drop terms. The single-phase pressure loss term is defined as the sum of single-phase dynamic and friction pressure losses in the sub-cooled length of the microchannel. The single-phase pressure loss term is represented by the following equation:

$$\Delta P_{sp} = \frac{\rho_f}{2}\left[\left(\frac{4f\mathrm{Re}L_{sub}}{D_h} + (K_c + K(\infty))\right)u_{ch}^2 + 2K_{90}u^2\right], \tag{2}$$

where u and u_{ch} are the mean velocity in the inlet manifold of the acrylic support and the microchannel, respectively. The contraction pressure loss coefficient (K_c), due to area contraction at microchannel's inlet is taken from Kays and London (1984). For the 90° bend pressure loss coefficient, Streeter (1961) recommended K_{90} to be 1.1 for macro-scale turbulent applications, and is not dependent on Reynolds number. The sub-cooled length can be calculated as

$$L_{sub} = \frac{\dot{m}C_p(T_{sat} - T_{in})}{q(2H_{ch} + W_{ch})N_{ch}}, \tag{3}$$

where T_{sat} is calculated based on the saturation pressure in the outlet manifold. The saturated length of the channel can be calculated as

$$L_{sat} = L_{ch} - L_{sub}. \tag{4}$$

For a single-phase fully developed laminar flow in rectangular channels with an aspect ratio, β, the friction factor can be defined by the following equation provided by Shah and London (1978)

$$f\mathrm{Re} = 24(1 - 1.3553\beta + 1.9467\beta^2 - 1.7012\beta^3 + 0.9564\beta^4 - 0.2537\beta^5). \tag{5}$$

Steinke and Kandlikar (2006) proposed the following equation to calculate Hagenbach's factor for the developing laminar length in terms of the microchannel aspect ratio

$$K(\infty) = 0.6796 + 1.2197\beta + 3.3089\beta^2 - 9.5921\beta^3 + 8.9089\beta^4 - 2.9959\beta^5, \tag{6}$$

The two-phase flow pressure drop in the saturated length of the microchannel is expressed as the sum of four components namely, frictional, acceleration, gravitational, and dynamic losses components as

$$\Delta P_{tp} = \Delta P_{tp,fr} + \Delta P_{tp,a} + \Delta P_{tp,gr} + \Delta P_{tp,dyn}, \tag{7}$$

The gravitational pressure drop component is far smaller than the frictional pressure drop component. Therefore, the effect of gravity can be reasonably neglected in microchannels. There have been numerous models and correlations developed to predict pressure drop in two-phase flows in horizontal pipes. Among the more common models are the homogeneous and the separated flow models. The homogeneous model assumes that the two-phase flow is a homogeneous mixture, where the liquid and vapor phases are sufficiently well mixed and are traveling at the same velocity with a weighted average property of each phase. The separated flow model considers the two-phases separately, with an inherent

Table 2
Test matrix used in the present study.

Parameter	Value
Mass flux	341–531 kg/m^2 s
Heat flux	60.4–130.6 kW/m^2
Inlet subcooling	2 °C
Exit quality	0.1–0.4

assumption that the two-phases reach constant but not necessarily equal velocities, e.g., vapor and liquid velocities. This assumption of different velocities is important when the densities of each phase are sufficiently different in the presence of large pressure gradients. The separated model is more appropriate in pressure drop predictions in microchannels than the homogeneous model because of considerable slip between the phases. The homogenous model can be used to predict the pressure drop in cases involving bubbly and churn flow patterns, which are rarely detected in microchannels. However, the slug, plug, and annular flow patterns are dominated where both flow phases are separated in these flow patterns.

Several pressure drop correlations have been proposed over the years, mostly based on experimental data. The method of calculations was based on the Lockhart and Martinelli (1949) analysis, which is a separated flow model. The Lockhart and Martinelli correlation appears to be the most current general model in the literature, although proprietary improvements have been made. They expressed the frictional two-phase flow pressure drop as

$$\left[\left(\frac{dP}{dL}\right)_{tp}\right]_{fr} = \phi_f^2\left[\left(\frac{dP}{dL}\right)_f\right]_{fr}, \tag{8}$$

Where ϕ_f^2 is the two-phase pressure drop multiplier defined as

$$\phi_f^2 = 1 + \frac{C}{X} + \frac{1}{X^2}, \tag{9}$$

where C is the two-phase multiplication factor. The liquid-phase pressure gradient is give by

$$\left(\frac{dP}{dL}\right)_f = f_f \frac{G^2(1-x_e)^2}{2\rho_f D_h}, \tag{10}$$

where

$$f_f = \frac{f\mathrm{Re}}{\mathrm{Re}_f}. \tag{11}$$

The Martinelli parameter, X^2, is defined as a function of the frictional pressure gradient assuming only liquid flow, and the frictional pressure gradient assuming only vapor flow, as is defined as:

$$X^2 = \left[\left(\frac{dP}{dL}\right)_f \Big/ \left(\frac{dP}{dL}\right)_g\right]_{fr}, \tag{12}$$

Eq. (8) expresses the two-phase frictional pressure drop in terms of the two-phase pressure drop multiplier and single-phase frictional pressure drop. This equation implies that the two-phase frictional pressure drop can be predicted if the two-phase pressure drop multiplier and single-phase frictional pressure drop are known. The acceleration pressure drop can be calculated from Zivi (1964)

$$\Delta P_{tp,a} = G^2 v_f \left[\frac{x_{e,o}^2}{\alpha_o}\frac{v_g}{v_f} + \frac{(1-x_{e,o})^2}{1-\alpha_o} - 1\right], \tag{13}$$

where α_o is defined as

$$\alpha_o = \frac{1}{1 + \left(\frac{1-x_{e,o}}{x_{e,o}}\right)\left(\frac{v_f}{v_g}\right)^{2/3}}. \tag{14}$$

The dynamic pressure losses of two-phase flow are due to the combined effects of two-phase dynamic losses in the microchannel's outlet due to area enlargement and bends. The two-phase pressure loss term due to the enlargement from the microchannel's outlet to the manifold is calculated using the following equations provided by Collier and Thome (1994):

$$\Delta P_{en,tp} = \frac{G^2 v_f}{2}(1-\sigma_{ch})^2\left[1 + x_{e,o}\left(\frac{v_{fg}}{v_f}\right)\right]. \tag{15}$$

On the other hand, Fitzsimmo (1964) reported that the pressure drop around bends for two-phase flow can be approximated as 2.5 times higher than that predicted using single-phase pressure loss measurements. The exit quality can be calculated using the heat balance equation taking in account the sub-cooled region as,

$$x_{e,o} = \frac{1}{h_{fg}}\left[\frac{Q_{net}}{\dot{m}} - C_p(T_{sat} - T_{in})\right]. \tag{16}$$

The net heat transferred to the fluid (Q_{net}) was determined as

$$Q_{net} = Q_{input} - Q_{loss}, \tag{17}$$

where Q_{loss} is the heat loss during the experiment and Q_{input} is the input power corresponds to Joule heating. The heat loss during the experiment can be expressed as

$$Q_{loss} = Q_{axial} + Q_{conv} + Q_{rad}, \tag{18}$$

where Q_{axial} is the heat loss due to axial heat conduction, and Q_{conv} and Q_{rad} are the heat dissipated due to heat losses by convection and radiation, respectively. The heat losses due to free convection and radiation were calculated first, then the heat loss due to axial conduction was determined as

$$Q_{axial} = \dot{m}C_p(T_{in} - T_{out}) - (Q_{conv} + Q_{rad}), \tag{19}$$

where T_{in} and T_{out} are the inlet and outlet temperatures measured at the inlet and outlet manifold based on a single-phase flow, respectively.

The primary heat loss present during the experiment amounts to the energy, which is not lost by convection to air or by radiation to the surrounding environment, but rather is lost via conduction to the heat sink support. The heat loss determined in this manner was 5.4% of the maximum heater power. Convection and thermal radiation losses are function of the heat sink surface temperature and are estimated to be less than 2.6% of the maximum power for all conditions. The convective heat loss is estimated by horizontal flat plate natural convection correlations. Radiation heat loss is calculated based on a horizontal black plate and the surroundings at the heat sink surface temperature with a radiation view factor equal to one. The net heat flux is found from the following equation:

$$q = \frac{Q_{net}}{A_{ch}}, \tag{20}$$

where A_{ch} is the microchannel heat transfer area for the three side heating, which can be expressed as:

$$A_{ch} = (2H_{ch} + W_{ch})L_{ch}N_{ch}, \tag{21}$$

3. Results and discussion

3.1. Flow visualization

The main objective of the flow visualization study is to provide insight into flow distribution, flow regimes, and transition characteristics in a parallel array of microchannels. The qualitative flow visualization results can be used to support the quantitative experimental data for better understanding of two-phase flow characteristics in microchannel heat sinks.

In order to check the manifold effect on the channels flow distribution, the flow patterns encountered in different channels at different time steps are shown in Fig. 6. Following flow patterns are encountered at $G = 341$ kg/m^2 s and $q = 130.6$ kW/m^2. In channels 21 and 22, slug flow can be clearly seen. The vapor phase is distributed as discrete slugs in a continuous liquid phase. The

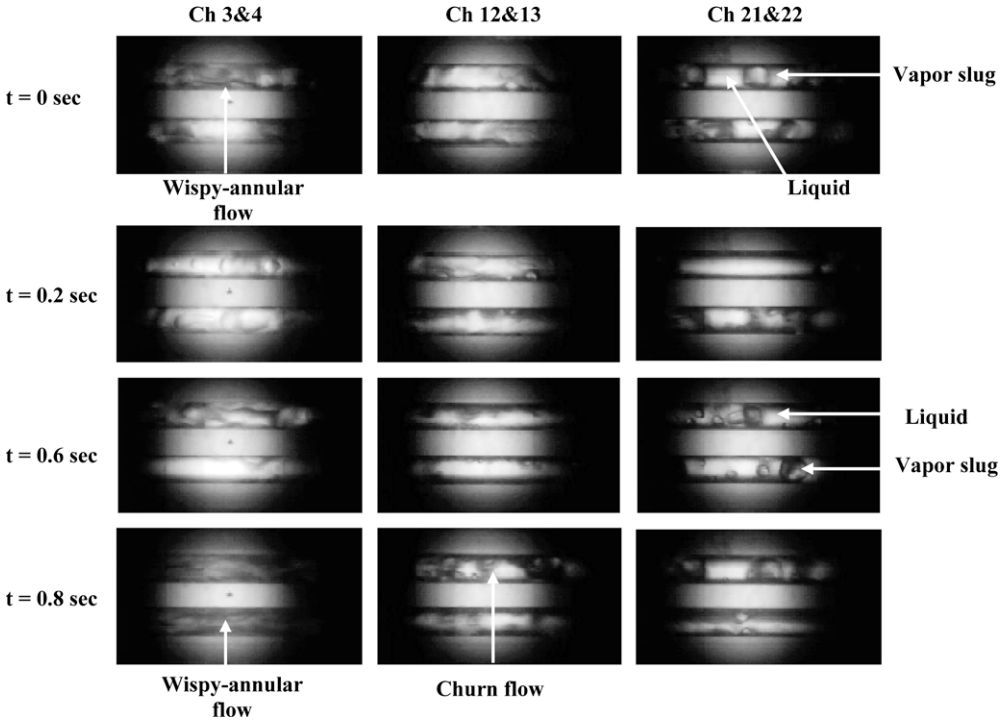

Fig. 6. Flow patterns observations for FC-72 at different microchannels at different time intervals, flow is from right to left for $G = 341$ kg/m^2 s and $q = 130.6$ kW/m^2 ($t = 0$ reference time).

vapor bubbles are approximately the diameter of the microchannel. Smaller entrained gas bubbles are also carried in the flow. These, images at different time steps, show the unsteady nature of two-phase flow.

Channels 12 and 13 show the transition from slug to churn flow, which is formed by the breakdown of the large vapor bubble in the slug flow. The flow has a time varying character. It can be concluded that the mass flux is unevenly distributed in the microchannels since different flow regimes exist at a constant heat flux (Cho and Cho, 2004).

Wispy-annular flow has been identified in channels 3&4. The flow in these two channels takes the form of a relatively thick liquid film on the walls of the channel together with a considerable amount of liquid entrained in a central vapor core. The liquid in the film is aerated by small gas bubbles and the entrained liquid phase appears as large droplets which have agglomerated into long irregular filaments or wisps. This region occurs at a lower mass flux.

This analysis indicates that different channels can simultaneously have different flow regimes, while constant mass flux and quality flow conditions are maintained. It is concluded that the distribution of two-phase flow between the channels is uneven and depends on the manifold configuration. Therefore, typical flow regime maps do not appear to be appropriate to describe the flow regimes, unless independent measurements of mass flux and quality are performed in each channel (Nino et al., 2003).

(Fig. 7) shows the observed flow patterns at the exit zone of the mid-channel of the heat sink for a constant mass flux of 341 kg/m^2 s and different exit quality. Three major flow patterns can be observed – bubbly flow, slug flow and annular flow, with annular flow being obtained at low exit quality.

Initiation of vapor bubble occurs at the preferred sites randomly distributed on the heated microchannel surface (Fig. 7a). As the exit quality increases, the bubble size increases while it is still attached to the wall (Fig. 7b). At a higher value of exit quality, the vapor bubble grows to a size at which the buoyancy force overcomes the surface tension force, acting at the line of attachment of the bubble to the wall. The bubble then departs from the surface and enters the liquid with a bubble diameter smaller than that of the

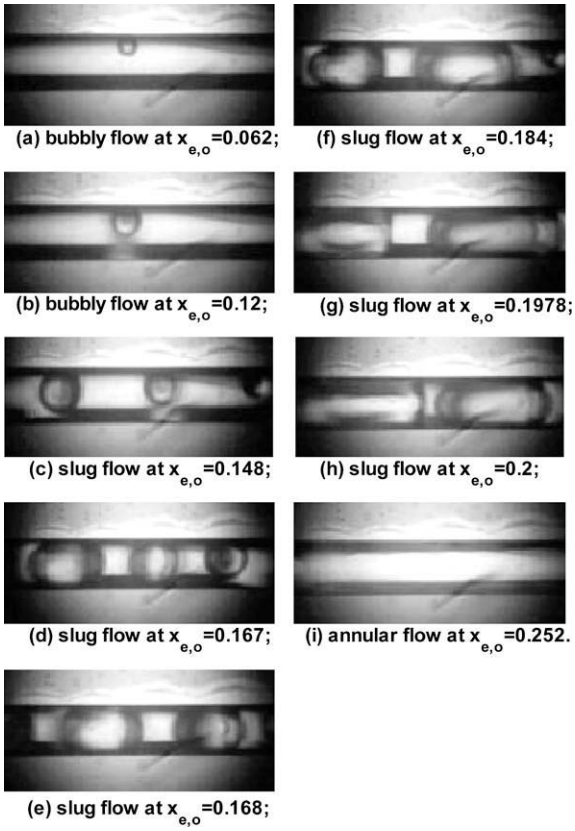

Fig. 7. Nucleation and flow patterns observations for FC-72 at the exit of the microchannels, flow is from right to left for $G = 341$ kg/m^2 s.

microchannel (Fig. 7c). Notably, bubbles are characterized by roughly spherical vapor regions surrounded by continuous liquid, and are distributed in the flow. An increase in exit quality increases the vapor bubble size. However, the geometry of the microchannel causes the vapor bubbles to be elongated after attaining their maximum size, which is the same diameter as the microchannel (Figs. 7d and e). It can also be noticed that slug flow does not result from the merging and coalescence of individual bubbles, but the bubbles are elongated and more cylindrical in shape. The elongated vapor bubbles are separated by liquid slugs.

Further increase in exit quality leads to further elongation of bubbles and also decreases the thickness of the liquid slug separating elongated bubbles (Figs. 7f–h). Additional increase in exit quality results in bubbles coalescence to form annular flow (Fig. 7i). In the annular flow, the gas occupies the central or core region of the microchannel, with the liquid remaining in a thin layer adjacent to the microchannel wall. Waves are presented on the liquid/gas interface and the instantaneous shape of the interface fluctuates with time. In their diabatic flow pattern map, Revellin and Thome (2007) observed that as the mass flux increases, the bubbly flow diminishes, and the transition from slug to annular flow takes place early at lower exit quality. These flow patterns and their transition characteristics match quite well with the flow visualization presented by Revellin and Thome (2007).

3.2. Pressure drop

(Fig. 8) shows the experimental results for the total pressure drop for five different mass fluxes. In general, the pressure drop increases as the exit quality and the mass flux increase. This is because the increasing of exit quality tends to increase both the acceleration and frictional losses for a constant mass flux. At low mass flux, it shows that increasing exit quality for a constant mass flux increases pressure drop up to a particular exit quality value beyond which the pressure drop increases slightly. As the mass flux increases, the pressure drop increases almost linearly with increasing exit quality due to a decrease in the vapor-to-liquid density ratio. The slope of the two-phase pressure drop starts to increase with an increase in the mass flux, as shown in Fig. 8.

The two-phase frictional pressure gradient is shown as a function of exit quality in Fig. 9. The experimental data indicates that when the exit quality is lower the pressure gradient increases sharply with the increase of vapor quality. The pressure drop increases almost linearly as the two-phase flow exit quality increases at low values of exit quality. However, a further increase in exit quality corresponds to a moderate increase of two-phase frictional pressure gradient.

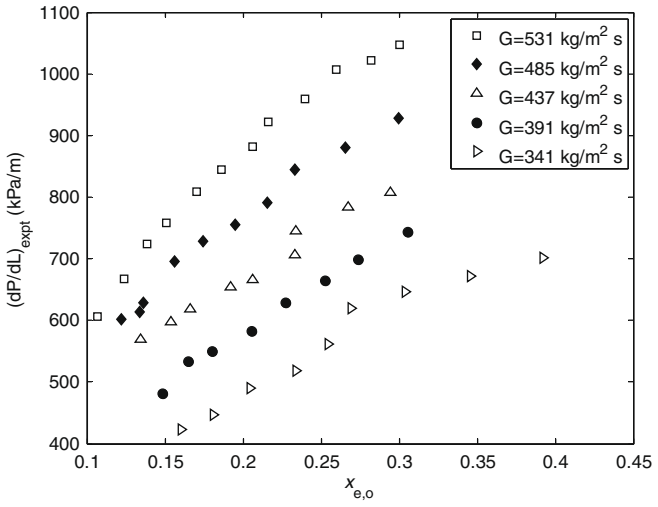

Fig. 8. Total pressure drop as a function of exit quality for different mass fluxes.

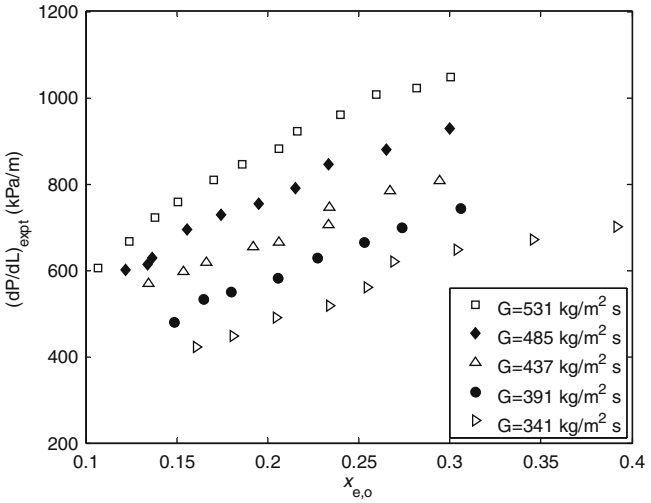

Fig. 9. Frictional pressure gradient as a function of exit quality for different mass fluxes.

3.3. Assessment of correlations

Although many correlations exist for two-phase flow in microchannels, their applicability to microchannels with a smaller diameter needs to be clarified. An experimental investigation assessed the accuracy of existing pressure drop correlations for two-phase flow in mini and microchannels, following the channels size ranges recommended by Kandlikar et al. (2001): microchannels (50–600 μm), minichannels (600 μm–3 mm) and conventional channels (D_h > 3 mm). These pressure drop correlations are based on the Lockhart and Martinelli (1949) analysis, which is a separated flow model. The Lockhart and Martinelli correlation seems to be the best current general model in the literature, although proprietary improvements have been made.

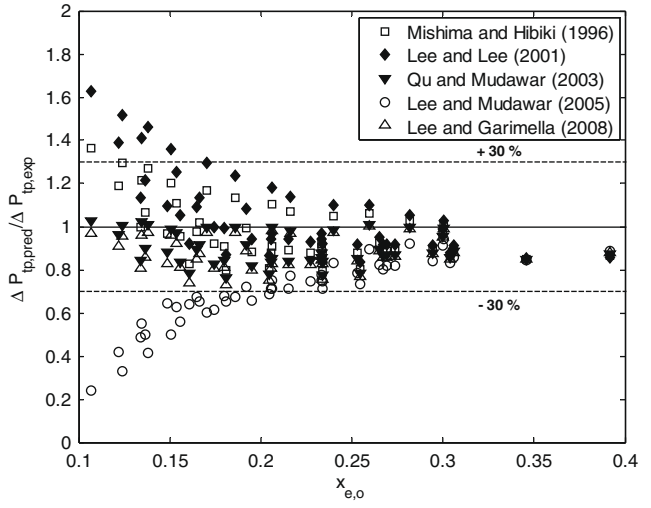

Fig. 10. Comparison of measured pressure drop data with predicted data from macro and microchannels correlations.

Table 3
Summary of two-phase pressure drop multiplication factors.

Reference	D_h (μm)	Two-phase multiplication factor	MAE (%)
Mishima and Hibiki (1996)	1000–4000	$C = 21(1 - e^{-319D_h})$	11.7
Lee and Lee (2001)	780–6670	$C = n\lambda^q\psi^r Re_{fo}^s$, $\lambda = \frac{\mu_f^2}{\rho_f \sigma D_h}$, $\psi = \frac{\mu_f j_f}{\sigma} n, q, r,$ and s from Table 4 in reference Lee and Lee, 2001	14.7
Qu and Mudawar (2003)	349	$C = 21(1 - e^{-319D_h})(0.00418G + 0.0613)$	10.4
Lee and Mudawar (2005)	349	Laminar-liquid–laminar-vapor: $C = 2.16Re_{fo}^{0.047}We_{fo}^{0.6}$ laminar-liquid turbulent-vapor: $C = 1.45Re_{fo}^{0.25}We_{fo}^{0.23}$	30.3
Lee and Garimella (2008)	160–538	$C = 2566G^{0.5466}D_h^{0.8819}(1 - e^{-319D_h})$	12.3
Megahed and Hassan (present study)	70–304	Laminar-liquid–laminar-vapor: $C = \frac{0.0053\mathrm{Re}_{fo}^{0.934}}{Co^{0.73}(X^2)^{0.175}}$	10.4
		Laminar-liquid turbulent-vapor: $C = \frac{0.0002\mathrm{Re}_{fo}^{1.7}}{Co^{0.7}(X^2)^{1.24}}$	14.5
		$Co = \frac{\left[\frac{\sigma}{g(\rho_f - \rho_v)}\right]^{\frac{1}{2}}}{D_h}$, $\mathrm{Re}_{fo} = \frac{GD_h}{\mu_f}$	

In (Fig. 10), pressure drop experimental data were compared with those calculated from the literature correlations presented in Table 3. The mean absolute error (MAE) was defined as:

$$\mathrm{MAE} = \frac{1}{N}\sum\left|\frac{\text{experimental data} - \text{predicted data}}{\text{experimental data}}\right| \times 100, \qquad (22)$$

where N is the total number of data points.

As (Fig. 10) shows, the Mishima and Hibiki (1996) correlation gives a good prediction based on the experimental data, although it was developed for conventional and mini tubes of D = 1–4 mm. This can be explained by the effect of tube size included in the correlation. The Lee and Lee (2001) correlation expressed the two-phase multiplication factor through dimensionless groups as a function of surface tension, viscosity, and inertia forces. Their correlation covers a wide range of conventional and mini size channels (780–6670 μm). It predicts the experimental data with a MAE of 14.7%. The Qu and Mudawar (2003) correlation gives the best prediction among the correlations tested with a MAE of 10.4%, as can be seen in Fig. 10. This can be attributed to the combined effect of both channel size and coolant mass flux incorporated in their correlations. Their correlations were developed based on microchannel pressure data with a hydraulic diameter of 349 μm.

The correlation by Lee and Mudawar (2005) allows calculating the pressure drop in terms of a two-phase multiplication factor as a function of an empirical combination of the liquid Reynolds and Weber numbers. The correlation has been developed by fitting the two-phase multiplication factor to 165 water and 87 R134a data points, collected by various authors, carried out in microchannels of D_h = 349 μm. They assumed that the pressure drop in slug and annular regimes is dominated by surface tension. It predicts the experimental data with high deviation as shown in Fig. 10. This can be explained by the difference in the working fluid properties. The surface tension of water is seven times higher than that of FC-72, which is used in the present study. However, the surface tension of R134a is almost the same as that of FC-72.

In a recent work Lee and Garimella (2008) have proposed a new correlation to predict the two-phase pressure drop in microchannels for D_h = 160–538 μm. However, their experimental data were presented at a very narrow band of exit quality (0.058–0.2). The two-phase pressure drop is expressed in terms of a two-phase multiplication factor, which is assumed to be a function of the hydraulic diameter and mass flux. The mathematical expression for the correlation is the result of a regression analysis applied to a data bank covering a wide range of liquid and gas flow rates.

In summary, in the ranges covered by the experiment ($x_{e,o}$ = 0.1–0.4 and q = 55–154 kW/m^2), all correlations agree with experimental results within 30% of the mean absolute error (MAE), except Lee and Mudawar's correlation. All data predicted by Qu and Mudawar (2003) and Lee and Garimella (2008) correlations are well within the error band and represent a mean absolute error of 10.4% and 12.3%, respectively.

3.4. New correlation

The frictional pressure drop has a significant contribution to the two-phase pressure drop in very small channels. Consequently, the frictional pressure drop in microchannels is expected to increase as the diameter decreases. Meanwhile, the acceleration pressure drop is expected to decrease as the diameter decreases. There have been a large number of exhaustive studies dealing with two-phase flow in microchannels with hydraulic diameters greater than 349 μm, and several correlations have been derived. Attempts are being made to develop prediction methods which are based on the separated model. The two-phase multiplier is correlated empirically, using the measured results, to mass flux, hydraulic diameter, and Reynolds and Weber numbers as shown in Table 3. All above-mentioned correlations still have reasonable deviation with the presented experimental data. The disagreement between measured pressure and predicted pressure drops using these methods can easily be 10% or more. The objective of the proposed correlation is to enhance the predictions of two-phase flow pressure drop correlations to cover laminar-liquid laminar-vapor and laminar-liquid turbulent-vapor flow in microchannels with smaller hydraulic diameters for different refrigerants.

In the present study, the two-phase multiplier parameter could be expressed by Lee and Lee (2001):

$$C = f(\mathrm{Re}_{fo}, Co, X^2) = c\mathrm{Re}_{fo}^{c_1} Co^{c_1}(X^2)^{c_3}, \qquad (23)$$

where Re_{fo} is Reynolds number assuming entire flow to be liquid, Co the confinement number, and X^2 is Martinelli parameter. The effect of confinement number is found to have a significant influence on correlation's predictions due to the effect of the buoyancy force. The multiplier in Eq. (23) is given as a function of the viscous, surface tension, inertia, as well as buoyancy forces. This method will be applicable to very small cross-section microchannel and to a wide range of density, surface tension, and viscosity values. The correlation evaluation was limited to three data sets since only two researchers provided enough information to calculate the frictional two-phase flow pressure gradient. Field (2007) presented data on the pressure drop during horizontal two-phase flow of R134a, propane, R410a, and ammonia in a microchannel heat sink with D_h = 148 μm. The mass flux ranges from 290 to 440 kg/m^2 s, and the exit quality from 0.01 to 0.96. Tu (2004) reported experiments on two-phase flow of R134a in microchannel heat sinks of 70, 104, 141, 150, and 304 μm hydraulic diameter, for mass flux values ranging from 102 to 785 kg/m^2 s and exit qualities from 0.01 to 0.95. A total of 324 data points were analyzed in the present study.

Table 4
Data used in the present study.

Case	Reference	Fluid(s)	D_h (μm)	G (kg/m^2 s)	$x_{e,o}$	Re_L	Re_g	X^2	No. of data points
Laminar-liquid–laminar-vapor	Present Study	FC-72	248	334–531	0.1–0.39	114–264	269–483	0.37–0.87	48
	Field (2007)	R134a, Propane, R410a, Ammonia	148	290–440	0.01–0.49	529–111	19–897	1.43–57.5	17
	Tu (2004)	R134a	70, 104, 141, 150, 304	102–785	0.01–0.75	30–545	27–992	1.8–95	112
Laminar-liquid–turbulent-vapor	Field (2007)	R134a, Propane, R410a, Ammonia	148	290–440	0.33–0.96	20–325	1036–3189	0.68–4.3	22
	Tu (2004)	R134a	70, 104, 141, 150, 304	102–785	0.21–0.95	17–452	1012–4443	1.8–5.4	125
	Summary	Five different refrigerants	70–304	102–785	0.01–0.96	17–545	19–4443	0.37–95	324

(Table 4) lists the experimental data collected from the literature. The data included two-phase pressure drop data for five different refrigerants with hydraulic diameter in the range of 70–304 μm. All refrigerant properties were obtained from NIST database (Chemistry WebBook). Based on the experimental data and using data regression techniques, the correlation for predicting the two-phase multiplier parameter could be obtained. (Table 3) presents the constants and parameters of the present correlation.

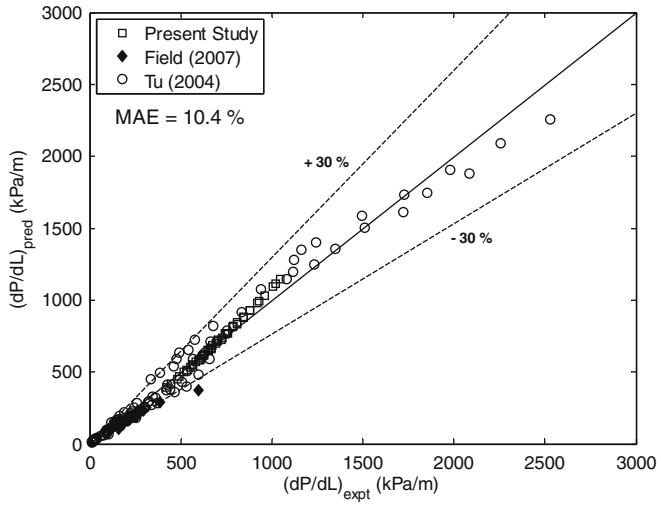

Fig. 11. Comparison of measured pressure drop data with predicted data for laminar-liquid laminar-vapor flow.

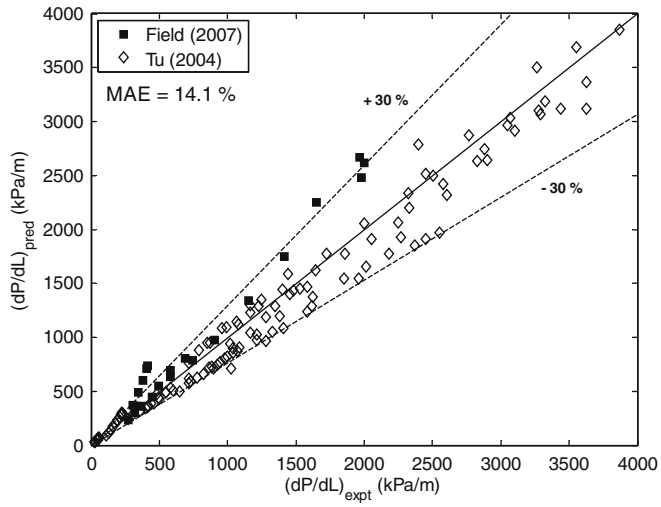

Fig. 12. Predicted values of two-phase pressure gradient with the new correlation against the experimental data for laminar-liquid–turbulent-vapor.

The predicted data, for laminar-liquid laminar-vapor case, have very good agreement with the experimental data. (Fig. 11) shows a comparison of the experimental data with predictions by the new correlation for laminar-liquid laminar-vapor. It is found that the pressure drop could be predicted by the correlation with a MAE of 10.4%. (Fig. 12) presents validation results of the new correlation versus the experimental data over a range of laminar-liquid turbulent-vapor flow. The new correlation predicts the experimental two-phase pressure drop data with a MAE of 14.5%.

4. Conclusion

Two-phase flow pressure drop measurements were investigated in a silicon microchannel heat sink. The pressure drop across the heat sink was related to the exit quality for different mass fluxes. The two-phase pressure drop depends strongly on the mass flux, and increases almost linearly with increasing exit quality at a constant mass flux. Flow visualization indicated that two-phase flow can be divided into three main flow regimes bubbly, slug, and annular. The experimental pressure drop data were compared with the predicted values of previously reported correlations in the literature to prove their validity. A new correlation for the prediction of the two-phase flow in microchannels is obtained from the present work employing different values of hydraulic diameter ranging from 70 to 304 μm and its applicability extends to five different refrigerants. The new correlation shows a good agreement with the experimental data and predicts the evaporative pressure drop data in microchannels for laminar-liquid laminar-vapor and laminar-liquid turbulent-vapor flow with mean absolute errors of 10.4% and 14.5%, respectively.

References

Balasubramanian, P., Kandlikar, S., 2005. Experimental study of flow patterns, pressure drop, and flow instabilities in parallel rectangular minichannel. Heat Transfer Eng. 26 (3), 20–27.
Bergles, A.E., 2003. Evolution of cooling technology for electrical, electronic, and microelectronic equipment. IEEE Trans. Compon. Packag. Technol. 26 (1), 6–15.
Cho, H., Cho, K., 2004. Mass flow rate distribution and phase separation of R-22 in multi-microchannel tubes under adiabatic condition. Microscale Thermophys. Eng. 8, 129–139.
Collier, J.G., Thome, J.R., 1994. Convective Boiling and Condensation. University Press, Oxford (Chapter 3).
Field, B.S., 2007. Two-Phase Pressure Drop and Flow Regime of Refrigerants and Refrigerant-Oil Mixture in Small Channels. Ph.D. Thesis, University of Illinois, Urbana-Champaign, IL.
Fitzsimmons, D.E., 1964. Two-phase pressure drop in piping components. HW 80970 Rev. 1.
Garimella, S.V., Chen, T., 2006. Measurements and high-speed visualizations of flow boiling of a dielectric fluid in a silicon microchannel heat sink. Int. J. Multiphase Flow 32 (8), 957–971.

Hetsroni, G., Klein, D., Mosyak, A., Segal, Z., Pogrebnyak, E., 2004. Convective boiling in parallel microchannels. J. Microscale Thermophys. Eng. 8 (4), 403–421.
Jiang, L., Wong, M., Zohar, Y., 2000. Phase change in microchannel heat sink under forced convection boiling. In: Proc. of the IEEE Micro Electro Mechanical Systems (MEMS), pp. 397–402.
Jiang, L., Wong, M., Zohar, Y., 2001. Forced convection boiling in a microchannel heat sink. J. Microelectromech. Syst 10 (1), 80–87.
Kandlikar, S.G., 2002. Fundamental issues related to flow boiling in minichannels and microchannels. Exp. Therm. Fluid Sci. 26 (2–4), 398–407.
Kandlikar, S.G., 2001. Two-phase flow patterns, pressure drop and heat transfer during boiling in minichannel and microchannel flow passages of compact heat exchangers. Compact Heat Exchangers and Enhancement Technology for the Process Industries, Begell House, New York, pp. 319–334.
Kays, W.M., London, A.L., 1984. Compact Heat Exchangers. McGraw-Hill, New York.
Kline, J., McClintock, F.A., 1953. Describing uncertainties in single-sample experiments. J. Mech. Eng. 75, 3–8.
Lee, P.S., Garimella, S.V., 2008. Saturated flow boiling heat transfer and pressure drop in silicon microchannel arrays. Int. J. Heat Mass Transfer 51 (3–4), 789–806.
Lee, H.J., Lee, S.Y., 2001. Pressure drop correlations for two-phase flow within horizontal rectangular channels with small heights. Int. J. Multiphase Flow 27 (5), 783–796.
Lee, J., Mudawar, I., 2005. Two-phase flow in high-heat-flux micro-channel heat sink for refrigeration cooling applications: part I-pressure drop characteristics. Int. J. Heat Mass Transfer 48 (5), 928–940.
Lee, M., Wong, Y.Y., Wong, M., Zohar, Y., 2003. Size and shape effects on two-phase flow patterns in microchannel forced convection boiling. J. Micromech. Microeng. 13 (1), 155–164.
Lockhart, R.W., Martinelli, R.C., 1949. Proposed correlation of data for isothermal two-phase, two-component flow in pipes. Chem. Eng. Prog. 45, 39–48.
Mishima, K., Hibiki, T., 1996. Some characteristics of air–water two-phase flow in small diameter vertical tubes. Int. J. Multiphase Flow 22, 703–712.
Muwanga, R., Hassan, I., MacDonald, R., 2007. Characteristics of flow boiling oscillations in silicon microchannel heat sinks. J. Heat Transfer 129 (10), 1341–1351.
Nino, V.G., Hrnjak, P.S., Newell, T.A., 2003. Two-phase flow visualization of R134A in a multiport microchannel tube. Heat Transfer Eng. 24 (1), 41–52.
NIST Chemistry WebBook. <http://webbook.nist.gov/>.
Qu, W., Mudawar, I., 2003. Measurement and prediction of pressure drop in two-phase micro-channel heat sinks. Int. J. Heat Mass Transfer 46, 2737–2753.
Revellin, R., Thome, J.R., 2007. A new type of diabatic flow pattern map for boiling heat transfer in microchannels. J. Micromech. Microeng. 17 (4), 788–796.
Shah, R.K., London, A.L., 1978. Laminar Flow Forced Convection in Ducts, Advances in Heat Transfer Supplement 1. Academic Press.
Steinke, M.E., Kandlikar, S.G., 2006. Single-phase liquid friction factors in microchannel. Int. J. Therm. Sci. 45 (11), 1073–1083.
Streeter, V.L., 1961. Handbook of Fluid Dynamics Edition, first ed. New York, McGraw-Hill.
Tu, X., 2004. Flow and Heat Transfer in Microchannels 30 to 300 Microns in Hydraulic Diameter. Ph.D. Thesis, University of Illinois, Urbana-Champaign, IL.
Tuckerman, D.B., Pease, R.F.W., 1981. High-performance heat sinking for VLSI. IEEE Electr. Dev. Lett. EDL-2 (5), 126–129.
Zivi, S.M., 1964. Estimation of steady-state stem void-fraction by means of the principle of minimum entropy production. ASME J. Heat Transfer 86, 247–252.